

AD-A113 312

STANFORD UNIV CA EDWARD L GINZTON LAB OF PHYSICS

F/6 14/5

ACOUSTIC MICROSCOPY AT CRYOGENIC TEMPERATURES.(U)

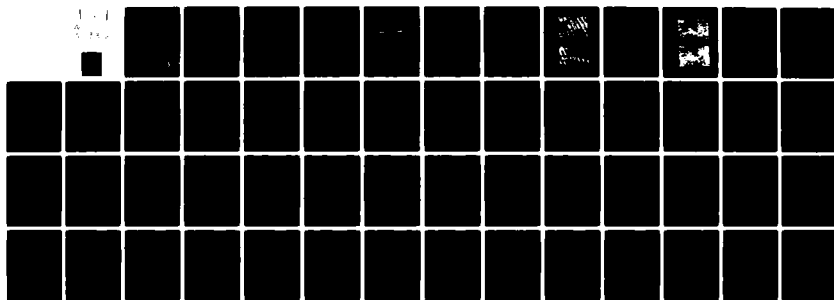
JAN 82 C F QUATE, J HEISERMAN

N00014-77-C-0412

UNCLASSIFIED

6L-3388

NL



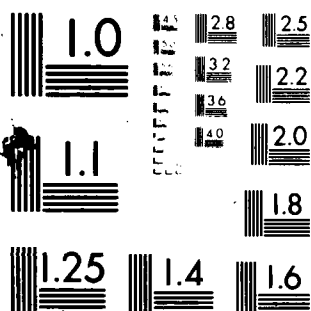
END

DATE

FILMED

5 82

DTIC



MICROCOPY RESOLUTION TEST CHART
NATIONAL BUREAU OF STANDARDS 1963-A

12

ACOUSTIC MICROSCOPY AT CRYOGENIC TEMPERATURES

AD A113312

Status Report

1 July 1981 - 1 January 1982

Contract No. N00014-77-C-0412

G.L. Report No. 3388

January 1982

Reproduction in whole or in part is permitted
for any purpose of the United States Government

DTIC FILE COPY

Edward L. Ginzton Laboratory
W.W. Hansen Laboratories of Physics
Stanford University
Stanford, CA 94305

DTIC
ELECTE
APR 13 1982
S E

82 04 12 147

UNCLASSIFIED

SECURITY CLASSIFICATION OF THIS PAGE (When Data Entered)

REPORT DOCUMENTATION PAGE		READ INSTRUCTIONS BEFORE COMPLETING FORM
1. REPORT NUMBER	2. GOVT ACCESSION NO.	3. RECIPIENT'S CATALOG NUMBER
	AD - A113312	
4. TITLE (and Subtitle)		5. TYPE OF REPORT & PERIOD COVERED
ACOUSTIC MICROSCOPY AT CRYOGENIC TEMPERATURES		Semiannual Status Report 1 July 81 - 1 January 82
7. AUTHOR(s)		6. PERFORMING ORG. REPORT NUMBER
C.F. Quate J. Heiserman		G.L. Report No. 3388
9. PERFORMING ORGANIZATION NAME AND ADDRESS		8. CONTRACT OR GRANT NUMBER(s)
Edward L. Ginzton Laboratory Stanford University Stanford, CA 94305		N00014-77-C-0412
11. CONTROLLING OFFICE NAME AND ADDRESS		10. PROGRAM ELEMENT, PROJECT, TASK AREA & WORK UNIT NUMBERS
Office of Naval REsearch Physics Division, Code 412 Arlington, Virginia 22217		Task NR384-924
14. MONITORING AGENCY NAME & ADDRESS (if different from Controlling Office)		12. REPORT DATE
		January 1982
		13. NUMBER OF PAGES
		51
		15. SECURITY CLASS. (of this report)
		UNCLASSIFIED
		15a. DECLASSIFICATION/DOWNGRADING SCHEDULE
16. DISTRIBUTION STATEMENT (of this Report)		
"Approved for public release; distribution unlimited"		
17. DISTRIBUTION STATEMENT (of the abstract entered in Block 20, if different from Report)		
18. SUPPLEMENTARY NOTES		
19. KEY WORDS (Continue on reverse side if necessary and identify by block number)		
Acoustic microscopy Superfluid helium Liquid argon Liquid nitrogen Mechanical scanning High frequency acoustic properties		
20. ABSTRACT (Continue on reverse side if necessary and identify by block number)		
During this six month period we completed construction of a mechanical scanning device compatible with our dilution refrigerator and suitable for use at very low temperatures. This device has now been thoroughly tested and was used to record our first acoustic images in liquid helium at temperatures below 0.1°K. This report describes the design of the mechanical scanner and presents the first micrographs taken in this new regime of imaging. We also present theoretical results which account for much of the nonlinear imaging behavior described in the previous status report. In particular we investigate the		

DD FORM 1473

1 JAN 73

EDITION OF 1 NOV 68 IS OBSOLETE
S/N 0102-LF 014-6601

UNCLASSIFIED

SECURITY CLASSIFICATION OF THIS PAGE (When Data Entered)

UNCLASSIFIED

SECURITY CLASSIFICATION OF THIS PAGE(When Data Entered)

20. (continued)

theory of resolution improvement when high acoustic intensities are used,
and quantitatively account for the onset of nonlinear excess attenuation.

Accession For	
NTIS GRA&I	<input checked="" type="checkbox"/>
DTIC TAB	<input type="checkbox"/>
Unannounced	<input type="checkbox"/>
Justification	
By	
Distribution/	
Availability Codes	
Dist	Avail and/or Special
A	



UNCLASSIFIED

SECURITY CLASSIFICATION OF THIS PAGE(When Data Entered)

A. INTRODUCTION

During this six-month period we completed construction of a mechanical scanning device compatible with our dilution refrigerator and suitable for use at very low temperatures. This device has now been thoroughly tested and was used to record our first acoustic images in liquid helium at temperatures below 0.1°K . This report describes the design of the mechanical scanner and presents the first micrographs taken in this new regime of imaging. We also present theoretical results which account for much of the nonlinear imaging behavior described in the previous status report.¹ In particular we investigate the theory of resolution improvement when high acoustic intensities are used, and quantitatively account for the onset of nonlinear excess attenuation.

B. LOW TEMPERATURE MECHANICAL SCANNER AND IMAGING RESULTS

In order to take advantage of the very low acoustic attenuation found in low temperature liquid helium, we have previously installed a dilution refrigerator capable of reaching temperatures down to about 0.015°K (15 mK). In the last six months we have constructed a mechanical scanner compatible with the dilution refrigerator and have produced the first microscopic images in very low temperature helium (< 100 mK). A schematic diagram of the scanner is shown in Figure 1. The scanner is bolted to the bottom of the dilution refrigerator mixing chamber. The sample is lowered through an experimental access tube which has been described previously.² The scanner moves the acoustic lens electromechanically in two dimensions by means of two drive coils oriented perpendicular to each other, and the

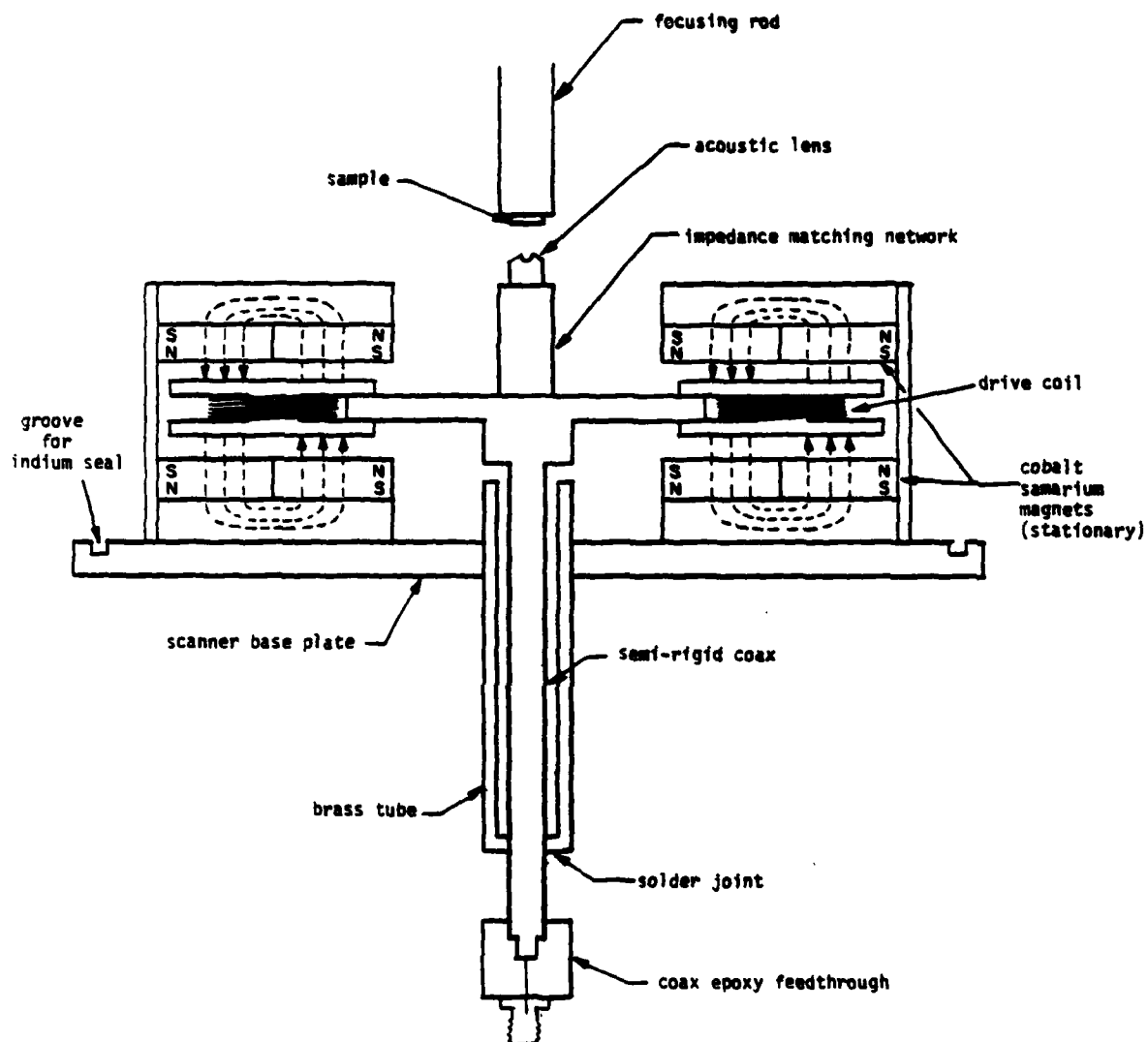


FIG. 1. Schematic diagram of mechanical scanner used in the very low temperature microscope.

motion is sensed by two additional coils. Only two of the four coils are shown in Figure 1. The lens is situated on a flexible post that is attached at the bottom of the scanner. A unique feature of this scanner is that the stainless steel semi-rigid coaxial line which transmits the microwave signals to and from the acoustic lens also acts as the flexible post (Uniform Tubes UT-141SS).

In operation, helium is condensed into the scanner and the whole apparatus is then cooled below 100 mK. To contain superfluid helium a leaktight design is required. This is achieved through the use of indium O-ring seals and a carefully constructed epoxy feedthrough for the coaxial line. One must also attempt to minimize the heat capacity of this large experimental package to allow cooling in a reasonable amount of time. Of particular concern is the very large specific heat of helium at low temperatures. For this reason we have reduced the helium volume of the scanner to less than 25 cm^3 by filling unoccupied space with nylon forms (not shown in Figure 1).

The performance of the scanner as evaluated in the first microscopic imaging experiment is impressive. After condensation of helium into the scanner, just 2-1/2 hours are required to cool to less than 50 mK. The accuracy of the raster scan was judged to be better than 1000 Å. Focusing of the sample was performed by a micrometer attached to the room temperature end of the sample holding rod and 1 micron positioning accuracy was observed. Some improvement of the focusing mechanism will be necessary in the future since the depth of focus will decrease when shorter acoustic wavelengths are used.

The lens used in the initial imaging experiment was described in a previous report.³ It has a radius of curvature of 80 μm and an opening angle of approximately 15° ($f/1.9$ aperture). A quarter wavelength layer of amorphous carbon serves as the acoustic impedance matching transformer. The frequency of operation is 980 MHz with a corresponding wavelength in the liquid of 2400 \AA . This is the shortest wavelength yet used for acoustic microscopy. The total insertion loss, including two-way transducer conversion loss, lens illumination loss and acoustic impedance mismatch loss, is approximately 53 dB. Despite this relatively low loss (room temperature microscopes typically operate with more than 90 dB of insertion loss), the signal-to-noise ratio of our imaging was less than 10 dB. The low signal-to-noise ratio is due to the large nonlinear attenuation which is encountered in the liquid path for rf input power greater than approximately -30 dBm (1 microwatt). Various methods of improving the signal-to-noise ratio are under consideration.

Two of the acoustic micrographs recorded between 50 and 80 mK are shown in Figure 2. The sample is a 4 μm period grating consisting of 2 μm wide aluminum lines on a glass substrate. The grating is seen only faintly in Figure 2(a) because the aluminum lines are very thin ($\approx 1000 \text{\AA}$) and because the depth of focus of our lens is rather large due to the small opening angle. The most prominent features in the image are the structures seen with black outlines. These regions are believed to consist of a thin layer of frozen air which selectively condenses onto the aluminum grating lines. The grating lines can be seen with greater contrast in Figure 2(b). The increased contrast is the result of operating the microscope in a highly nonlinear regime. The

→ | 4 μ m | ←



(a)



(b)

FIG. 2. Images taken in liquid at approximately 0.05°K. The object is a 4 μ m period grating consisting of aluminum lines on glass.

details of this contrast enhancing effect are not yet understood.

In future experiments we plan to further improve the mechanical components of our apparatus, such as the focusing mechanism, and to increase our frequency of operation to 2.5 GHz ($\lambda = 950 \text{ \AA}$). The acoustic lens for this higher frequency has been fabricated, though it has not yet been tested in liquid helium.

C. THEORY OF NONLINEAR RESOLUTION IMPROVEMENT

In the previous status report¹ we described the discovery of a nonlinear acoustic effect which increases the resolving power of the reflection acoustic microscope beyond the linear diffraction limit. This effect is observed when the acoustic intensity in the liquid is sufficiently high for significant harmonic generation to take place. Depletion of the fundamental frequency by 90% or more is commonly achieved in our experiments. Although the generated harmonics are believed to play an essential role in the observed resolution improvement, only the fundamental frequency is transmitted and received by the microscope.

The resolution improvement which accompanies high intensity imaging is demonstrated in Figure 3. The object shown is an etched glass grating with 2000 \AA spatial period. The images were taken in liquid argon at 2.0 GHz with an acoustic wavelength of 4300 \AA . Figure 3(a) is the image which is seen when the microscope is operated in the linear (low power) regime; the grating is not visible since its spatial period is smaller than can be theoretically detected. When the rf input power is increased by 14 dB, the image in Figure 3(b) results. The grating is now clearly visible, indicating increased imaging resolution. The grating defects are also seen



(a)

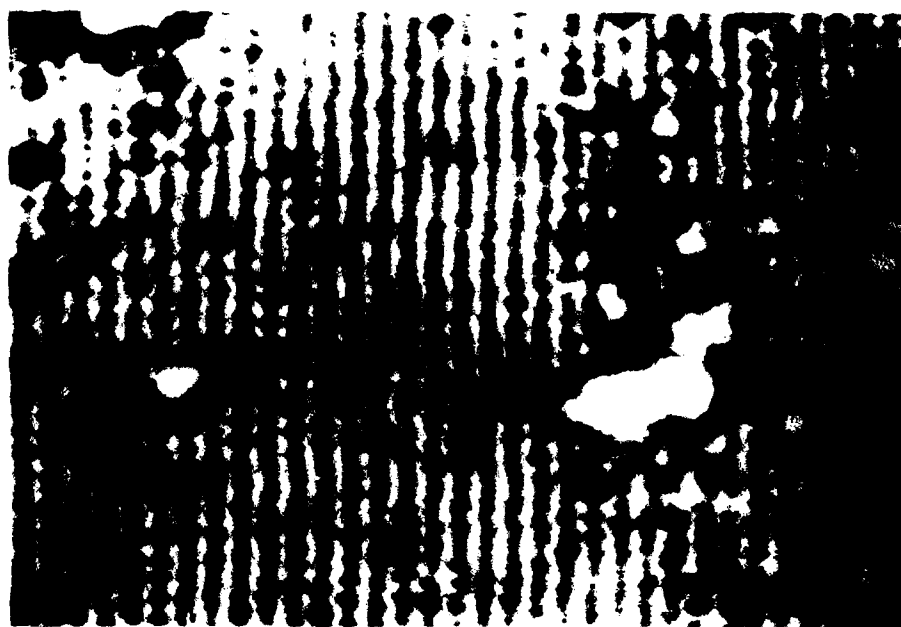


FIG. 3. Images of a 2000 Å period grating taken in liquid argon at 2.0 GHz ($\lambda = 4300 \text{ Å}$). Image (a) is taken at low power (linear regime), while image (b) is taken at higher power (nonlinear regime).

with greater sharpness, a further indication that the point response of the microscope has been improved by operating in the nonlinear regime.

The details of our experimental findings were presented in the previous report. In this report we provide the theoretical basis for understanding the origin of the nonlinear resolution improvement. We will also quantitatively account for the experimentally observed nonlinear excess attenuation of the fundamental and explain why nonlinear effects are relatively more important in cryogenic liquids than in water. After a brief review of nonlinear acoustics, we consider the case of second harmonic generation in a gaussian focused beam. In this model we ignore depletion of the fundamental and generation of harmonics higher than the second. Despite these deficiencies, the behavior of nonlinear focused beams is elucidated. The second case we consider is the propagation of finite amplitude converging spherical waves. A numerical solution of the problem is obtained which takes into account the depletion of the fundamental and generation of harmonics higher than the second.

C.1 Nonlinear Acoustics — Background

It is found both experimentally and theoretically that pressure peaks of finite amplitude waves propagate faster than the pressure troughs. This causes a wave which is initially sinusoidal to distort as it propagates. Such a wave will approach the shape of a sawtooth wave in the limit of high amplitude or, if there is no loss, long propagation distance. The importance of such nonlinear effects is governed by the size of the particle velocity relative to the speed of sound (the acoustic Mach number), the nonlinearity of the equation of state, the distance over which the sound travels and the acoustic attenuation of the liquid.

An important length scale in nonlinear acoustics is the discontinuity length. This is the distance at which, in the absence of attenuation, the slope of a portion of the waveform becomes infinite. The discontinuity length is given by

$$L = \left[(1 + B/2A) \frac{\omega v_0}{c_0^2} \right]^{-1} = \frac{1}{\beta M k} \quad (1)$$

where $\omega = 2\pi f$ is the angular frequency, v_0 is the peak particle velocity, $k = \omega/c_0$, $M = v_0/c_0$ is the acoustic Mach number and $\beta = (1 + B/2A)$. The quantity B/A is determined by the nonlinearity of the equation of state of the liquid. For water at 60°C, $B/A = 5.7$.⁴ For liquid nitrogen at its normal boiling point, $B/A = 6.6$.⁴

To convert from acoustic intensity to an acoustic Mach number, the following relation is useful

$$I = \frac{1}{2} Z v_0^2, \quad (2)$$

where I is the acoustic intensity (power per unit area) and $Z = \rho_0 c_0$ is the acoustic impedance. We may then write

$$\begin{aligned} M = v_0/c_0 &= (2I/Z)^{1/2}/c_0 \\ &= \left(\frac{2I}{\rho_0 c_0^3} \right)^{1/2} \end{aligned}$$

Thus we see that high acoustic Mach numbers are more easily generated in media with low acoustic velocity and low acoustic impedance. This is an important point since cryogenic liquids have these properties.

Table 1 gives the Mach number and discontinuity length for liquid nitrogen and water at several different acoustic power levels. At 1000 W/cm^2 in water the Mach number is 0.002. For the same power level, liquid nitrogen has the value $M = 0.006$. This value is higher than in water because of the lower acoustic impedance and propagation velocity of nitrogen.

Attenuation has the effect of counteracting the formation of shock waves in the liquid. The nonlinear distortion of the wave is equivalent to the generation of higher harmonics. Since attenuation in most liquids increases as ω^2 , the higher harmonics will be attenuated more rapidly than the fundamental. This tends to restore the waveform to its original sinusoidal form. Nonlinear effects in lossy liquids become important when the discontinuity length is smaller than the attenuation length. This is parameterized by Γ , the Gol'berg number

$$\Gamma = 1/\alpha L \quad .$$

Nonlinear effects are important for $\Gamma > 1$. Some representative values of the Gol'berg number are given in Table 1.

It is found experimentally that the fundamental frequency component of a high amplitude wave suffers greater attenuation than does a low amplitude wave. Blackstock⁵ has examined in detail the phenomenon of nonlinear excess attenuation of the fundamental for plane waves. The nonlinear attenuation is due to the depletion of energy in the fundamental by the generation of harmonics. For propagation of plane waves over distances much greater than L , the excess attenuation is determined solely by Γ . In particular, Blackstock showed that for long propagation paths the excess attenuation is approximately given by

TABLE 1
Nonlinear Plane Wave Propagation in Water and Liquid Nitrogen

H_2O (60°C)

$$B/A = 5.7$$

$$f = 2.6 \text{ GHz}$$

$$\lambda = 0.60 \text{ } \mu\text{m}$$

$$1/\alpha = 13 \text{ } \mu\text{m}$$

$I(W/cm^2)$	M	L	Γ	Excess Attenuation *
100	0.0007	34 μm	0.38	0 dB
1000	0.0023	11 μm	1.2	0.3 dB
10,000	0.0073	3.4 μm	3.8	3 dB
100,000	0.023	1.1 μm	12	10 dB

LIQUID NITROGEN

$$B/A = 6.6$$

$$f = 2.6 \text{ GHz}$$

$$\lambda = 0.33 \text{ } \mu\text{m}$$

$$1/\alpha = 11 \text{ } \mu\text{m}$$

$I(W/cm^2)$	M	L	Γ	Excess Attenuation *
10	0.0006	19 μm	0.5	0 dB
100	0.0020	6.1 μm	1.8	0.9 dB
1000	0.0064	1.9 μm	5.8	5 dB
10,000	0.020	0.61 μm	18	14 dB
100,000	0.064	0.19 μm	58	23 dB

* Calculated for propagation over path much longer than L .

$$\text{EXDB} = -20 \log_{10} \left[\frac{4I_1(r/2)}{rI_0(r/2)} \right],$$

where EXDB is the nonlinear excess attenuation in decibels. The functions I_0 and I_1 are Bessel functions of imaginary argument. For $r = 1$, the excess attenuation is 0.27 dB. For $r = 10$, it is 8.9 dB.

One conclusion to be drawn from plane wave analysis is that lower intensity is required in liquid nitrogen than in water for nonlinear effects to be important. For example, at 2.6 GHz the power required for $r = 1$ is 910 W/cm² in water and 31 W/cm² in liquid nitrogen.

While nonlinear propagation of plane waves is well understood, the propagation of focused beams has not been as thoroughly investigated. The principle work on this subject has been done by Beyer,⁴ Muir,⁶ Naugol'nykh et al.,⁷ Bakhvalov et al.,⁸ and Sutin,⁹ among others. In addition to these acoustic studies, work done on nonlinear generation in focused optical beams is relevant. The work by Kleinman, Ashkin, and Boyd¹⁰ on second harmonic generation in gaussian optical beams is found to be particularly useful.

To understand the properties of focused beams, a mathematical basis for solving nonlinear wave propagation problems is needed. The equations of nonlinear acoustics have been derived by various investigators.^{11,7,12} A recent work by Tjøtta and Tjøtta¹¹ derives the nonlinear wave equation from the Navier-Stokes hydrodynamic equations and makes logical connection with equations derived by others. The relationship of equations by Westervelt,¹² Blackstock,⁵ Kuznetsov,¹³ and Zabolotskaya and Khokhlov¹⁴ is discussed in Reference 11. The analysis in the remainder of this report is based on the

equation

$$\left(\nabla^2 - \frac{1}{c_0^2} \frac{\partial^2}{\partial t^2} \right) \rho = - \frac{D}{c_0^4} \frac{\partial^3 \rho}{\partial t^3} \quad (3)$$

$$- \frac{\beta}{\rho_0 c_0^2} \frac{\partial^2}{\partial t^2} (\rho - \rho_0)^2$$

where, as before, $\beta \equiv (1 + B/2A)$. This equation was derived by Tjøtta and Tjøtta and is similar to that used by Westervelt.¹² The first term on the right side of (3) is the attenuation term. The quantity D is given by

$$D = \left(\frac{4}{3} \eta + \zeta \right) + \left(\frac{1}{C_v} - \frac{1}{C_p} \right) \kappa$$

where η is the shear viscosity, ζ is the bulk viscosity, κ is the thermal conductivity, C_v is specific heat at constant volume and C_p is specific heat at constant pressure. The second term on the right side of (3) is the nonlinear term and leads to nonlinear distortion of the waveform and harmonic generation.

In order to find a solution to (3) we must specify the boundary condition

$$\rho(x,y,z,t) \Big|_{\substack{x,y,z \text{ on} \\ \text{surface } S}}$$

For the acoustic microscope the surface S of the boundary condition is the spherical lens-liquid interface. The amplitude and phase of the acoustic

source at this surface is determined by the pupil function of the lens.

C.2 Second Harmonic Generation in Focused Gaussian Acoustic Beams

We consider here second harmonic generation (SHG) in a focused beam under the assumptions of no depletion of the fundamental beam and no generation of harmonics higher than the second. The amplitude profile of the fundamental beam is assumed to be gaussian. The gaussian beam is a good approximation of the true beam shape in the focal region and has the advantage that an analytical expression for beam propagation is easily written.

We start with Eq. (3) and decompose the density variation into a fundamental wave (frequency ω_1) and a second harmonic wave (frequency $\omega_2 = 2\omega_1$)

$$\rho = \text{Re} \left[\rho_0 + \rho^{(1)}(x,y,z)e^{-i\omega_1 t} + \rho^{(2)}(x,y,z)e^{-i\omega_2 t} \right] , \quad (4)$$

where $\rho^{(1)}(x,y,z)$ and $\rho^{(2)}(x,y,z)$ are complex-valued functions describing the amplitude and phase of the two waves.

If we substitute (4) into (3) and equate terms of like frequency, we get two equations

$$(\nabla^2 + k_1^2)\rho^{(1)} = -2i \frac{\omega_1}{c_0} \alpha_1 \rho^{(1)} \quad (5)$$

$$\begin{aligned} (\nabla^2 + k_2^2)\rho^{(2)} &= -2i \frac{\omega_2}{c_0} \alpha_2 \rho^{(2)} \\ &\quad + \frac{2\beta}{\rho_0} \frac{\omega_1^2}{c_0^2} \left(\rho^{(1)} \right)^2 , \end{aligned} \quad (6)$$

where $k_1 = \omega_1/c_0$ and $k_2 = 2k_1 = \omega_2/c_0$.

The first equation is just the lossy wave equation for the fundamental wave. There is no nonlinear term in this equation since we have assumed that the fundamental is undepleted and therefore unaffected by the nonlinear processes. The second equation is the lossy wave equation for the second harmonic with a nonlinear source term which accounts for generation of the second harmonic.

For notational convenience we rewrite Eq. (6) as

$$(\nabla^2 + k_2^2)\rho^{(2)} = -i2k_2\alpha_2 + \gamma(\rho^{(1)})^2 \quad (7)$$

where

$$\gamma \equiv \frac{2\beta}{\rho_0} \frac{\omega_1^2}{c_0^2} .$$

In the absence of loss ($\alpha_2 = 0$), Eq. (7) can be solved using a Green's function:

$$\rho^{(2)}(x,y,z) = \gamma \int_{z_0}^z \int_{-\infty}^{\infty} \int_{-\infty}^{\infty} G(\vec{r}, \vec{r}') \left(\rho^{(1)}(\vec{r}')\right)^2 dx' dy' dz' \quad (8)$$

where z_0 is the coordinate specifying where the wave enters the nonlinear medium and is assumed to be fixed. The Green's function is given by

$$G(\vec{r}, \vec{r}') = \frac{1}{4\pi} \frac{e^{ik_2 R}}{R} , \quad (9)$$

where

$$R = |\vec{r} - \vec{r}'| .$$

The vectors \vec{r} and \vec{r}' are given in terms of unit vectors as

$$\vec{r} = x\hat{x} + y\hat{y} + z\hat{z}$$

and

$$\vec{r}' = x'\hat{x} + y'\hat{y} + z'\hat{z} .$$

A Green's function solution essentially identical to the one above was used by Ingenito and Williams¹⁵ in their analysis of SHG for a plane piston radiator. In an analysis of parametric acoustic interaction, Westervelt¹² used a similar integral expression.

To analyze gaussian focused beams it will prove useful to modify the Green's function by the paraxial approximation. The new Green's function takes the form

$$G(\vec{r}, \vec{r}') = \frac{1}{4\pi} \frac{1}{Z} \exp \left(ik_2 Z + ik_2 (x^2 + y^2) / 2Z \right) \quad (10)$$

where

$$X = x - x'$$

$$Y = y - y'$$

$$Z = z - z' > 0 .$$

It was assumed that $x^2 + y^2 \ll Z^2$ so that we could write

$$R \approx Z + (x^2 + y^2)/2Z$$

in the exponential.

If loss is included, the paraxial Green's function is modified further:

$$G(\vec{r}, \vec{r}') = \frac{1}{4\pi} \frac{1}{Z} \exp \left(-\alpha_2 Z + ik_2 Z + ik_2 (x^2 + y^2)/2Z \right) . \quad (11)$$

This Green's function is essentially the same as the one used by Kleinman, Ashkin, and Boyd¹⁰ in their analysis of optical SHG.

To analyze harmonic generation in focused beams we start with a gaussian fundamental beam

$$\rho^{(1)}(x, y, z) = \rho_{10} \frac{e^{-\alpha_1 z}}{1 + i\xi} e^{ik_1 z} \exp \left[-\frac{x^2 + y^2}{w_0^2(1 + i\xi)} \right] , \quad (12)$$

where $\xi = 2(z - f)/b$ is a dimensionless quantity parameterizing propagation distance and $b = w_0^2 k_1$ is the confocal length. The function in (12) describes a focused acoustic beam whose cross-section at all z positions has a gaussian amplitude distribution. It is well known that such a function is a paraxial solution to the wave equation.^{10,16} The width of the beam, defined as the radial distance at which the amplitude of the beam falls to $1/e$ of its on-axis value, takes on the minimum value w_0 at the focus ($z = f$).

From (12) the intensity of the beam (power per unit cross-sectional area) is given by

$$\begin{aligned} I^{(1)}(x, y, z) &= \frac{c_0^3}{2\rho_0} |\rho^{(1)}(x, y, z)|^2 \\ &= \frac{c_0^3}{2\rho_0} |\rho_{10}|^2 \frac{e^{-2\alpha_1 z}}{1 + \xi^2} \exp \left(-\frac{2(x^2 + y^2)}{w_0^2(1 + \xi^2)} \right) \end{aligned} \quad (13)$$

and the total power in the beam is

$$\begin{aligned}
 p^{(1)}(z) &= \iint_{-\infty}^{\infty} I^{(1)}(x,y,z) dx dy \\
 &= \frac{c_0^3}{2\rho_0} |\rho_{10}|^2 e^{-2\alpha_1 z} \left(\frac{\pi w_0^2}{2} \right) \quad (14)
 \end{aligned}$$

One important physical feature of the gaussian beam solution is the phase shift which occurs upon passage through the focal region. The phase of the focused beam relative to a plane wave changes along the propagation path due to the factor $1/(1 + i\xi)$ in (12). From this factor it can be seen that the phase of the field at the focus ($\xi = 0$) is shifted by $\pi/2$ relative to the phase of the converging wave ($\xi \ll 0$). The diverging wave ($\xi \gg 0$) is π out of phase with the converging wave.

To find the second harmonic beam, we square the fundamental field (12) and use the integral solution (8) with the Green's function in (11). Following the procedure of Kleinman, Ashkin and Boyd,¹⁰ we get

$$\begin{aligned}
 \rho^{(2)}(x,y,z) &= \rho_{10}^2 (\gamma/4\pi) \int_{z_0}^z \int_{-\infty}^{\infty} \int_{-\infty}^{\infty} \frac{\exp(-2\alpha_1 z' + i2k_1 z)}{Z(1 + i\xi')^2} \\
 &\quad \times \exp \left[\frac{-2(x'^2 + y'^2)}{w_0^2(1 + i\xi')} \right] \exp(-\alpha_2 Z + ik_2(x^2 + y^2)/2Z) dx' dy' dz' , \quad (15)
 \end{aligned}$$

where $\xi' = 2(z' - f)/b$ and $k_2 = 2k_1$.

The x' integral in (15) can be written as

$$I_{x'} = \int_{-\infty}^{\infty} \exp \left[\frac{-2x'^2}{w_0^2(1+i\xi')} + \frac{ik_2x'^2}{2Z} \right] dx' \quad (16)$$

Expanding x'^2 in the exponential,

$$I_{x'} = \exp \left[\frac{ik_2x'^2}{2Z} \right] \times \int_{-\infty}^{\infty} \exp \left[-\frac{ik_2xx'}{Z} - i \left(-\frac{k_2}{2Z} - \frac{i2}{w_0^2(1+i\xi')} \right) x'^2 \right] dx' .$$

The coefficient of x'^2 in the parentheses can be written as

$$q = -\frac{k_1(1+i\xi)}{Z(1+i\xi')} .$$

Letting the coefficient of x' in the integral be written as

$$p = \frac{k_2x}{Z} ,$$

we now make use of the relation¹⁰

$$\int_{-\infty}^{\infty} \exp(-ipx - iqx^2) dx = \left(\frac{\pi}{iq} \right)^{1/2} \exp(ip^2/4q) .$$

This relation is true if $\text{Im}(q) < 0$, a condition which holds here since $\xi' < \xi$. We get for (16)

$$I_{x'} = \left(\frac{i\pi Z(1+i\xi')}{k_1(1+i\xi)} \right)^{1/2} \exp \left(-\frac{2x^2}{w_0^2(1+i\xi)} \right)$$

A similar procedure is followed for evaluation of the y' integral in (15).

Using the above results, the solution for the second harmonic wave (15) becomes

$$\rho^{(2)}(x,y,z) = \rho_{20}(z) \frac{\exp(i2k_1 z)}{1 + i\xi} \exp\left[-\frac{2(x^2 + y^2)}{w_0^2(1 + i\xi)}\right] \quad (17)$$

where

$$\rho_{20}(z) = i\rho_{10}^2 \frac{\gamma}{4k_1} e^{-\alpha_2 z} \int_{z_0}^z \frac{\exp[-(2\alpha_1 - \alpha_2)z']}{1 + i\xi'} dz' \quad (18)$$

From (17) we see that the second harmonic beam has the amplitude cross section and phase curvature of a gaussian focused beam. The amplitude and phase of the beam is modified from that of a freely propagating gaussian beam, however, due to the multiplying function $\rho_{20}(z)$.

From Eq. (17) we also deduce the important result that the width of the beam at the focus is $w_0/\sqrt{2}$. This is a factor of $\sqrt{2}$ smaller than the width of the fundamental beam and is consistent with the experimental finding that resolution improves by a factor of at least 1.4 when imaging is done at high power.

By analogy to Eqs. (13) and (14), the intensity of the second harmonic beam is

$$I^{(2)}(x,y,z) = |\rho_{20}(z)|^2 \frac{1}{1 + \xi^2} \exp\left[-\frac{4(x^2 + y^2)}{w_0^2(1 + \xi^2)}\right] \quad (19)$$

and the total power in the beam at a given z plane is

$$p^{(2)}(z) = \frac{c_0^3}{2\rho_0} |\rho_{20}(z)|^2 \left(\frac{\pi w_0^2}{4} \right) \quad (20)$$

C.2.1 Power content of second harmonic beam -- lossless case

From Eq. (20) we see that the power in the second harmonic beam is proportional to the quantity $|\rho_{20}(z)|^2$. In the case of no loss, $\rho_{20}(z)$ is given by

$$\rho_{20}(z) = i \rho_{10}^2 \frac{\gamma}{4k_1} S(z) \quad (21)$$

where

$$S(z) = \int_{z_0}^z \frac{dz'}{1 + i\xi'}$$

Writing this integral as the sum of real and imaginary parts, we get

$$S(z) = S_R(z) + i S_I(z)$$

where

$$S_R(z) = \int_{z_0}^z \frac{1}{1 + \xi'^2} dz' \quad (22)$$

and

$$S_I(z) = - \int_{z_0}^z \frac{\xi'}{1 + \xi'^2} dz' \quad (23)$$

These integrals are easily integrated to give

$$S_R = \frac{b}{2} (\tan^{-1} \xi - \tan^{-1} \xi_0) \quad (24)$$

and

$$S_I = -\frac{b}{4} \log \left(\frac{1 + \xi^2}{1 + \xi_0^2} \right) , \quad (25)$$

where

$$\xi_0 = 2(z_0 - f)/b . \quad (26)$$

From (5.26) and (5.27), the power in the second harmonic beam is

$$P^{(2)}(z) = C|S|^2 = C(S_R^2 + S_I^2) ,$$

where

$$C = \frac{\pi}{128} \frac{C_0^3}{\rho_0} w_0^2 \frac{\gamma^2}{k_1^2} |\rho_{10}|^4 .$$

If the definition of γ in (7) is used,

$$C = \frac{\pi}{32} \frac{C_0}{\rho_0^3} B^2 \omega_1^2 w_0^2 |\rho_{10}|^4 . \quad (27)$$

We now consider an example pertinent to acoustic microscopy and assume the following parameters:

$$f = 0 \text{ } \mu\text{m}$$

$$z_0 = -18 \text{ } \mu\text{m}$$

$$-18 < z < 18 \text{ } \mu\text{m}$$

$$w_0 = 0.55 \lambda$$

$$\lambda = 0.326 \mu\text{m}$$

These parameters represent the case of an 18 μm radius acoustic lens operating at 2.6 GHz in liquid nitrogen. The corresponding values for ξ and ξ_0 are

$$\xi_0 = -57.9$$

$$\xi_0 < \xi < 57.9$$

Plots of S_R^2 (dashed line), S_I^2 (dotted line) and $|S|^2 = S_R^2 + S_I^2$ (solid line) are shown in Fig. 4. The plots were computed using (24) and (25). We see that S_R^2 grows in the region $\xi < 0$, peaks at the focus ($\xi = 0$) and diminishes in the diverging region of the beam ($\xi > 0$). The function S_I^2 grows most rapidly near the focus and then remains constant in the diverging beam. The combination of the two contributions, $S_R^2 + S_I^2$, represents the total second harmonic power in the beam. It starts with zero value initially ($\xi = -57.9$) and builds up to a peak just past the focus at $\xi = 0.6$. As the beam diverges ($\xi > 0$), the total power in the second harmonic beam decays to a finite value.

We now consider the feeding of power from the fundamental beam to the second harmonic and vice versa. The change in power content of the fundamental wave as it propagates is not directly calculated since we are using a model which ignores depletion (and growth) of the fundamental. If the propagation is lossless, however, we can infer the transfer of power out of and back into the fundamental by observing the growth and decay of the second

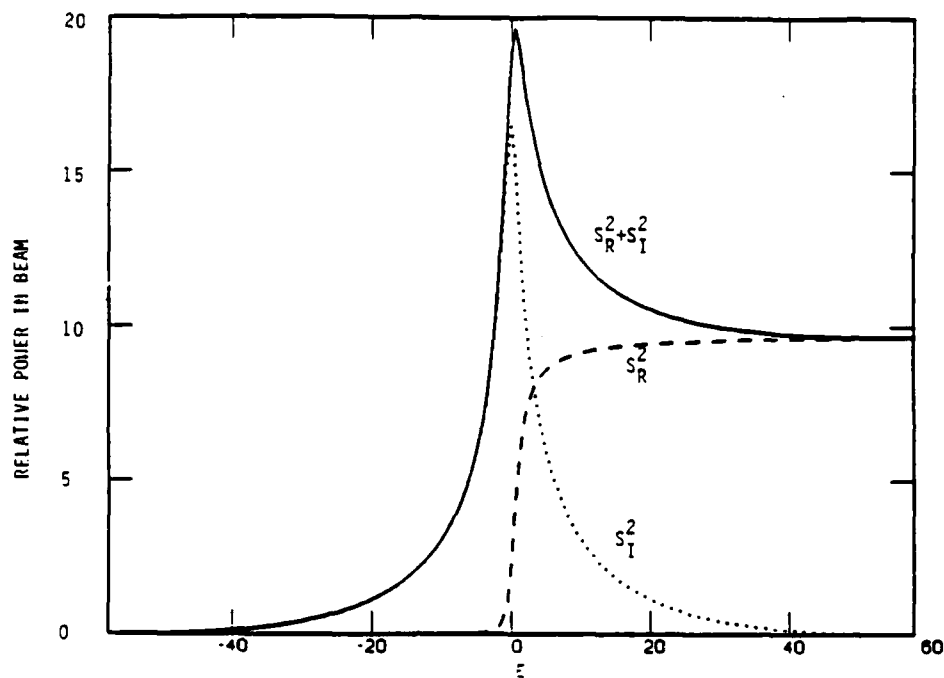


FIG. 4 Second harmonic beam power as a function of distance for lossless liquid. The variable ξ parameterizes the distance and equals zero at the focus.

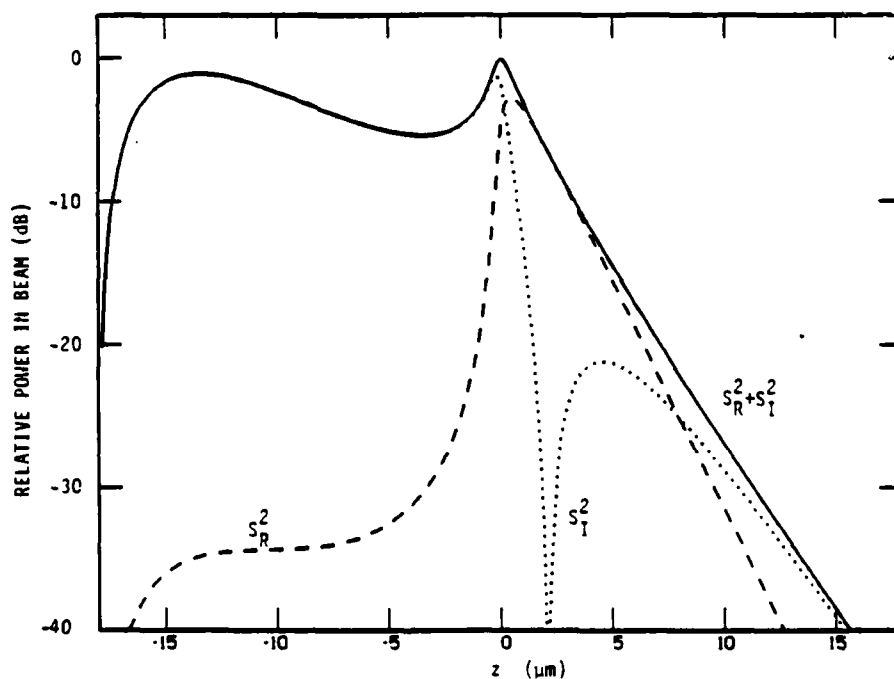


FIG. 5 Second harmonic beam power as a function of distance for lossy liquid. The assumed parameters correspond to 18 μm radius lens operating in liquid nitrogen at 2.6 GHz. The focus corresponds to $z=0$.

harmonic. By conservation of energy or, equivalently, by the Manley-Rowe relations of parametric processes, we know that the sum of the power in the two beams is constant. On the converging side of the focus ($\xi < 0$), the harmonic content of the beam steadily rises as the beam propagates toward the focus (see the solid line in Fig. 4). In this region, power is fed from the fundamental wave into the second harmonic beam. After peaking at $\xi \approx 0.6$, the second harmonic power decreases 49% when propagating from $\xi = 0$ to $\xi = 57.9$. This means that 49% of the power in the second harmonic beam at the focus is converted back into power at the fundamental frequency. This down conversion is responsible for the communication of high resolution information to the fundamental frequency.

C.2.2 Power content of second harmonic beam -- lossy case

In the previous section we examined second harmonic generation for a gaussian fundamental propagating in a lossless medium. In this section we examine the same case but include the effects of loss. As in the previous case, the power in the second harmonic beam is determined by $|\rho_{20}(z)|^2$. Following the same procedure as in the preceding section, we get

$$p^{(2)}(z) = C|S|^2 = C(S_R^2 + S_I^2)$$

where

$$S_R = \text{Re}(S) ,$$

$$S_I = \text{Im}(S) ,$$

and the quantity S is defined as

$$S(z) = e^{-\alpha_2 z} \int_{z_0}^z \frac{\exp -[(2\alpha_1 - \alpha_2)z']}{1 + i\xi'} dz' , \quad (28)$$

where α_1 and α_2 are amplitude attenuation constants for the fundamental and second harmonic, respectively. This definition of $S(z)$ reduces to the one in (21) if $\alpha_1 = \alpha_2 = 0$. The integral in (28) may be integrated numerically.

To illustrate the behavior of second harmonic power $p^{(2)}(z)$, we consider the same parameters as used in Section C.2.1. In addition, we must specify the loss parameters. We choose attenuation numbers appropriate for liquid nitrogen at 2.6 GHz:

$$\alpha/f^2 = 13.8 \times 10^{-15} \text{ sec}^2/\text{m}$$

$$\alpha_1 = 9.3 \times 10^4 \text{ m}^{-1}$$

$$\alpha_2 = 3.7 \times 10^5 \text{ m}^{-1}$$

Figure 5 shows plots of S_R^2 (dashed line), S_I^2 (dotted line) and $|S|^2 = S_R^2 + S_I^2$ (solid line). We see that the harmonic power (as measured by $|S|^2$) grows rapidly in the vicinity of the transmitting lens and reaches a broad local maximum at $z \approx -14 \mu\text{m}$. The harmonic power then decreases somewhat before rising to a sharp second peak near the focus ($z = 0$). After the focus the harmonic power rapidly diminishes due to the strong absorption.

The lossy case differs from the lossless case in several important respects. In the lossless case, the focal region is the principle site of nonlinear generation. In the lossy case, although the focus is still important, we find that the region near the lens in the neighborhood of

$z = -15 \mu\text{m}$ is also a site of significant nonlinear interaction. The dominance of the focus has been reduced by the attenuation in the liquid of the fundamental beam. Another significant difference between the lossy and lossless cases lies in the relative importance of S_R^2 and S_I^2 . In the lossless case, S_I^2 is the dominant contribution to total harmonic power in the converging beam, while S_R^2 is the dominant contribution in the diverging beam. In the lossy case, we see from Fig. 5 that S_I^2 dominates in both the converging beam and in the diverging beam for $z > 10 \mu\text{m}$. S_R^2 dominates only in the region $0 < z < 7 \mu\text{m}$. In this region we note that S_I^2 goes through a sharp null. We mention these features because of their similarity with the solutions obtained using an analysis of spherical wave propagation.

C.3. Nonlinear Spherical Wave Analysis

In the previous section the nonlinear properties of the focused acoustic beam were analyzed by considering second harmonic generation due to an undepleted gaussian beam at the fundamental frequency. This model was adequate for determining that the spot size of the second harmonic beam was smaller than that of the fundamental by a factor of $\sqrt{2}$ and for demonstrating that a portion of the power in the second harmonic beam is fed back to the fundamental upon passage through the focal region.

In this section we consider an alternative model. We consider the propagation of a finite amplitude spherical wave, taking into account absorption, depletion of the fundamental and generation of harmonics higher than the second. The neglected effects in this analysis are diffraction and nonlinear interaction at the focus. Far from the focal region the omission of diffraction effects is not a serious problem. However, when the wave approaches to within one confocal parameter of the focus, diffraction becomes

important and the true solution deviates from the spherical wave solution. This deficiency is the same one encountered by Sutin in his analysis of focused beams in a lossless medium.⁹ In his analysis, Sutin ignored nonlinear effects for propagation within one confocal parameter of the focus. A similar assumption will be made in this section. We assume that propagation from one side of the focal region to the other occurs without nonlinear interaction; only linear attenuation of harmonics is taken into account. The focal region is defined as $-b < r < b$ where $b = 2\pi w_0^2/\lambda$ and w_0 is the $1/e$ radius of the focal spot.

The assumption of no nonlinear interaction in the focal region is a significant limitation to this theory since it is in this region that the intensity is highest. However, the assumption is not as bad as it may seem for two reasons. First, the presence of relatively high attenuation tends to reduce the intensity at the focus and de-emphasize its importance, as was seen in Fig. 5. Secondly, harmonic generation is a cumulative effect and the distance through the focal region is short (typically only a few wavelengths for the acoustic microscope). We discuss further the effect of ignoring nonlinear interaction at the focus in Section C.3.5.

C.3.1 Equations for finite amplitude spherical waves

The analysis of nonlinear spherical waves begins with Eq. (3) which we rewrite here as

$$\left(\nabla^2 - \frac{1}{c_0^2} \frac{\partial^2}{\partial t^2} \right) \rho = - \frac{D}{c_0^4} \frac{\partial^3 \rho}{\partial t^3} - \frac{B}{\rho_0 c_0^2} \frac{\partial^2}{\partial t^2} (\rho - \rho_0)^2 \quad (29)$$

We assume a general solution including all harmonics

$$\rho = \frac{1}{2} \left[\rho_0 + \rho_1(r) e^{i(k_1 r - \omega_1 t)} + \rho_2(r) e^{i(k_2 r - \omega_2 t)} + \rho_3(r) e^{i(k_3 r - \omega_3 t)} + \dots \right] \quad (30)$$

+ complex conjugate ,

where $\omega_n = n\omega_1$, $k_n = nk_1$ and the $\rho_n(r)$ are complex valued functions representing harmonic amplitudes. We now expand the last term of Eq. (29)

$$(\rho - \rho_0)^2 = \frac{1}{2} \sum_{j=1}^{\infty} \rho_j \rho_j^* + \frac{1}{4} \sum_{n=1}^{\infty} \left[\sum_{j=1}^{n-1} \rho_j \rho_{n-j} + 2 \sum_{j=1}^{\infty} \rho_{n+j} \rho_j^* \right] e^{i(k_n r - \omega_n t)}$$

+ complex conjugate of previous term .

Therefore,

$$-\frac{\beta}{\rho_0 c_0^2} \frac{\partial^2}{\partial t^2} (\rho - \rho_0)^2 = \frac{\beta}{\rho_0 c_0^2} \frac{1}{4} \sum_{n=1}^{\infty} \omega_n^2 \times \left[\sum_{j=1}^{n-1} \rho_j \rho_{n-j} + 2 \sum_{j=1}^{\infty} \rho_{n+j} \rho_j^* \right] e^{i(k_n r - \omega_n t)}$$

+ c.c. (31)

Substituting (31) into (29) and equating terms with like propagation factors, we get the system of equations

$$\begin{aligned} & \left(\nabla^2 - \frac{1}{c_0^2} \frac{\partial^2}{\partial t^2} \right) \left(\rho_n(r) e^{i(k_n r - \omega_n t)} \right) \\ &= -i 2 \frac{\omega_n}{c_0} \alpha_n \left(\rho_n(r) e^{i(k_n r - \omega_n t)} \right) \\ &+ \frac{\beta}{\rho_0 c_0^2} \frac{\omega_n^2}{2} \left(\sum_{j=1}^{n-1} \rho_j \rho_{n-j} + 2 \sum_{j=1}^{\infty} \rho_{n+j} \rho_j^* \right) e^{i(k_n r - \omega_n t)}. \end{aligned} \quad (32)$$

The Laplacian on the left hand side of (32) can be approximated as

$$\begin{aligned} & \nabla^2 \left(\rho_n(r) e^{i(k_n r - \omega_n t)} \right) \\ &= \left[\frac{2ik}{r} \rho_n - k^2 \rho_n + 2ik \frac{\partial}{\partial r} \rho_n \right] e^{i(k_n r - \omega_n t)} \end{aligned} \quad (33)$$

where we have used the slowly varying envelope approximation

$$k_n \rho_n \gg \frac{\partial \rho_n}{\partial r}$$

and

$$k_n \frac{\partial \rho_n}{\partial r} \gg \frac{\partial^2 \rho_n}{\partial r^2}.$$

Substituting (33) into (32) yields

$$\frac{\partial \rho_n(r)}{\partial r} + \frac{\rho_n(r)}{r} = -\alpha_n \rho_n(r) \quad (34)$$

$$- \frac{i \beta \omega_n}{4 \rho_0 c_0} \left(\sum_{j=1}^{n-1} \rho_j \rho_{n-j} + 2 \sum_{j=1}^{\infty} \rho_{n+j} \rho_j^* \right) .$$

Equation (34) is the basic equation for the propagation of spherical waves in a nonlinear medium. For computational purposes, however, it is useful to make a change of variable so that the loss and geometrical focusing terms in the differential equations are eliminated. Let

$$\rho_n(r) = \frac{\rho_0}{c_0} \frac{r_0}{r} e^{-\alpha_n(r-r_0)} G_n(r) \quad (35)$$

If this is substituted into (34), a simplified system of equations is obtained

$$\begin{aligned} \frac{\partial G_n}{\partial r} = & - \frac{i \beta \omega_n}{4 c_0^2} \frac{r_0}{r} e^{\alpha_n(r-r_0)} \\ & \left[\sum_{j=1}^{n-1} G_j G_{n-j} \exp[-(\alpha_j + \alpha_{n-j})(r - r_0)] \right. \\ & \left. + 2 \sum_{j=1}^{\infty} G_{n+j} G_j^* \exp[-(\alpha_j + \alpha_{n+j})(r - r_0)] \right] . \end{aligned} \quad (36)$$

Using the relation

$$\sum_{j=1}^{n-1} G_j G_{n-j} = \frac{2}{n} \sum_{j=1}^{n-1} j G_j G_{n-j}$$

we get

$$\frac{\partial G_n}{\partial r} = - \frac{i\beta\omega_1}{2C_0^2} \frac{r_0}{r} \exp(\alpha_n(r - r_0))$$

$$\left\{ \sum_{j=1}^{n-1} j G_j G_{n-j} \exp[-(\alpha_j + \alpha_{n-j})(r - r_0)] \right. \quad (37)$$

$$\left. + n \sum_{j=1}^{\infty} G_{n+j} G_j^* \exp[-(\alpha_j + \alpha_{n+j})(r - r_0)] \right\}$$

This complex set of equations is equivalent to the two real sets of equations derived by Trivett and Van Buren.¹⁷

C.3.2 Calculation of harmonic amplitudes in liquid nitrogen

If the harmonic amplitudes $G_n(r)$ are specified at the boundary $r = r_0$, a finite subset of the infinite set of equations in (37) can be numerically solved to find the harmonic amplitudes at the other values of r . Equation (35) is used to convert from $\rho_n(r)$ to $G_n(r)$ and vice versa. A computer program using a quartic Runge-Kutta technique was written to numerically integrate (37).

Trivett and Van Buren¹⁷ discuss the numerical solution of equations similar to those in (37). They note that the principle problem in using a truncated set of equations is the build up of amplitude in the highest included harmonic. In the examples presented below, seven harmonics are included in the calculations. The strong acoustic attenuation of the seventh harmonic prevents excessive amplitude from accumulating in this harmonic due

to the truncation. The integration step-size was chosen to be 0.05 times the discontinuity length as calculated by (1). This was found to give better than 1% accuracy for the harmonic amplitudes, a finding consistent with the results of Reference 17.

The diagram in Fig. 6 is useful for understanding the calculations. An initial intensity is specified at the lens surface, designated by radius r_0 . The corresponding value for $G_1(r_0)$ is found using (2) and (37). The initial amplitude of $G_n(r_0)$ for $n > 1$ is zero. Equations (37) are step-wise integrated to find the growth (or decay) of the harmonics. The integration stops when $r = r_1$. This is the boundary of the focal region, determined by the confocal length b . The amplitudes $\rho_n(r_1)$ are then propagated across the focal region according to

$$\rho_n(r_2) = - \rho_n(r_1) \exp[- \alpha_n(r_2 - r_1)] \quad (38)$$

where r_2 is the radius of the other side of the focal region. Equation (38) takes into account linear absorption and a change in sign due to the π phase shift at the focus. The propagation from r_2 back to the lens at r_3 is carried out by further integration of (37).

The following numerical values are used in the calculation

$$\begin{aligned} r_0 &= -18 \text{ } \mu\text{m} \\ r_1 &= -b \\ r_2 &= b \\ r_3 &= 18 \text{ } \mu\text{m} \\ b &= 2\pi w_0^2/\lambda = 0.622 \text{ } \mu\text{m} \\ w_0 &= 0.55 \lambda \end{aligned}$$

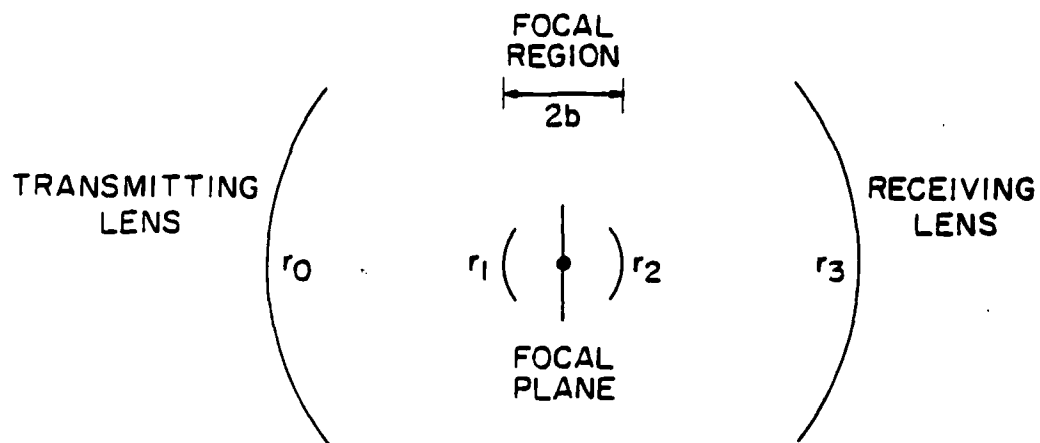


FIG. 6. Geometry for nonlinear spherical wave analysis. Wave is launched from transmitting lens at radius r_0 and propagates according to nonlinear spherical wave equations until radius r_1 . In the focal region (radius r_1 to r_2), nonlinear interaction is ignored and the wave propagates taking into account linear attenuation of harmonics and a π phase shift. From radius r_2 to the receiving lens at r_3 , the wave propagates according to nonlinear wave equations.

$$\lambda = 0.327 \text{ } \mu\text{m}$$

$$\alpha_n = n^2 \times 9.3 \times 10^4 \text{ m}^{-1}$$

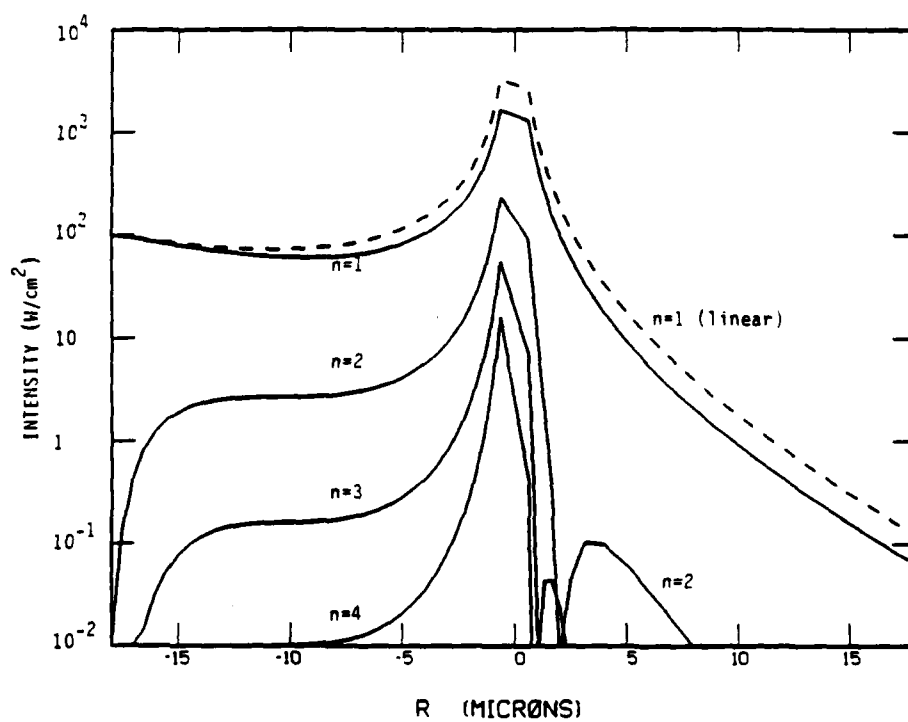
$$B/A = 6.6$$

It should be mentioned here that the size of the lens opening angle affects the calculations only indirectly by determining the value of w_0 and, thereby, the confocal length, b . The value of w_0 indicated above corresponds to an opening half angle of 53° .

Figure 7 shows the results of calculations for the case of an $18 \text{ } \mu\text{m}$ radius lens operating in liquid nitrogen at 2.6 GHz. The intensity of the fundamental wave at the transmitting lens surface ($r = -18 \text{ } \mu\text{m}$) was chosen to be 100 W/cm^2 . The plot in Fig. 7(a) shows how the intensities of the first four harmonics vary along the propagation path. The dashed line shows the intensity that the fundamental wave would have as a function of radius if the propagation were linear. It is seen that at this intensity level the strength of the fundamental wave follows the linear result closely. It is observed that the intensity of the fundamental is almost constant for $-18 \text{ } \mu\text{m} < r < -5 \text{ } \mu\text{m}$. In this region the intensifying effect of geometrical focusing is approximately balanced by acoustic absorption. For $-5 \text{ } \mu\text{m} < r < 0$, the effect of focusing is larger than attenuation and thus the intensity rises to a peak to the focus. The deviation of the fundamental wave intensity from that of the linear case is due to depletion of the fundamental by harmonic generation. At the exit from the liquid ($r = 18 \text{ } \mu\text{m}$), the excess attenuation of the fundamental due to this effect is seen to be 3.5 dB.

The plot in Fig. 7(b) is similar to Fig. 7(a) except that power in the beam is displayed rather than intensity. Thus the linear case, depicted by the dashed line, shows a steady exponential decline of beam power as a

(a) 2.6 GHZ NITRØGEN 100 W/CM SQ



(b) 2.6 GHZ NITRØGEN 100 W/CM SQ

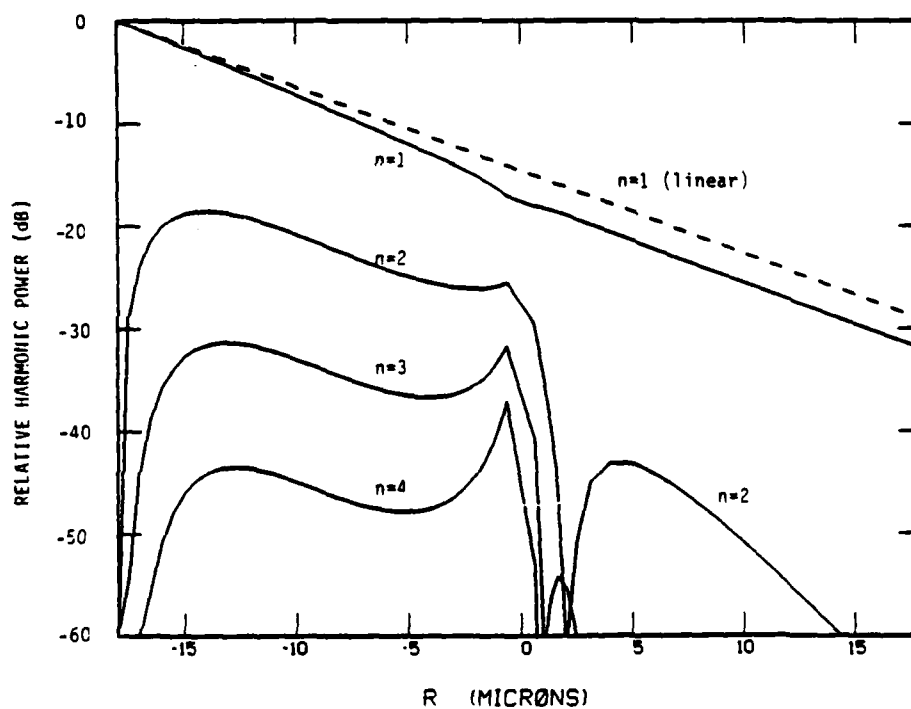
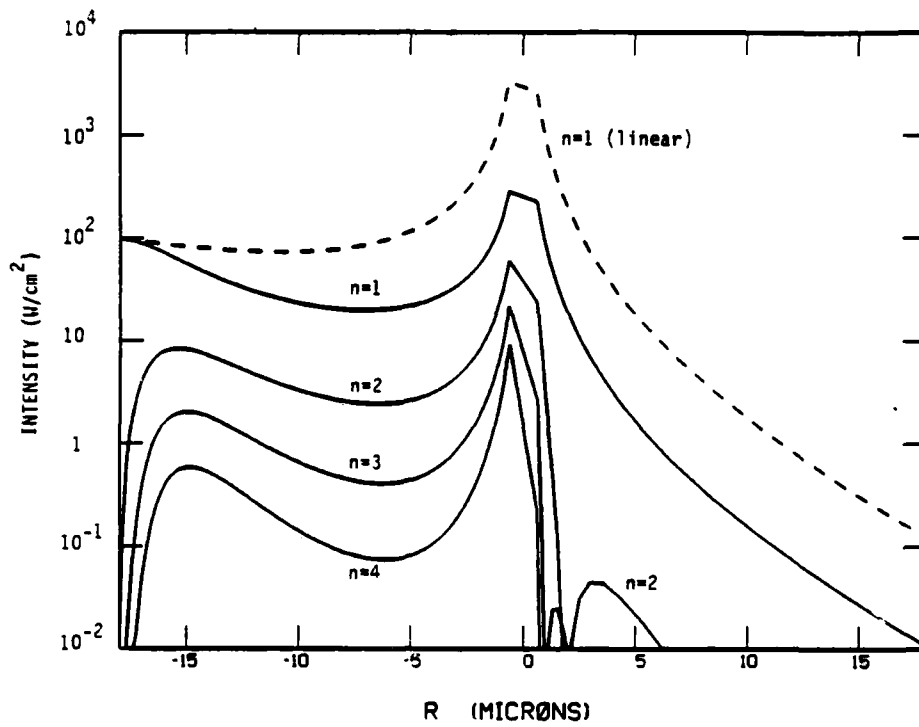


FIG. 7. Propagation of spherical waves in nitrogen for initial intensity of $100 \text{ W}/\text{cm}^2$. Plot (a) shows intensity of harmonics up to the 4th and (b) shows the power in the beam.

function of radius due to absorption instead of the peaked response shown in the previous plot. One feature of interest in Fig. 7(b) is the build up of second harmonic power in the vicinity of the transmitting lens. This result is similar to the gaussian beam result in Fig. 5. Another interesting feature of Fig. 7(b) is the behavior of the second harmonic in the diverging region of the beam ($r > 0$). It is seen that after reaching a maximum in the focal region, the second harmonic power declines rapidly and goes through zero at $r \approx 2 \mu\text{m}$. This is due to the feeding of energy from the second harmonic back to the fundamental and is similar to the behavior observed in the S_I^2 contribution in gaussian beams (see Fig. 5). After going through zero, power again builds up in the second harmonic but with reversed phase. It should be noted that the zero which occurs in the second harmonic power is an artifact of ignoring nonlinear interaction in the focal region. This is discussed further in Section C.3.5 where the spherical wave and gaussian beam results are compared in more detail.

The plots in Fig. 8 and Fig. 9 are similar to those in Fig. 7 except that different initial intensities are assumed. In Fig. 8 the initial intensity is 1000 W/cm^2 while in Fig. 9 the assumed intensity is $10,000 \text{ W/cm}^2$. It is seen that as the initial intensity is increased, the build up of harmonics near the transmitting lens takes place more rapidly. Also, it is evident that the higher transmitted intensity results in greater excess attenuation of the fundamental, as expected. For the case of 1000 W/cm^2 , the excess attenuation at $r = 18 \mu\text{m}$ is 11.4 dB. For $10,000 \text{ W/cm}^2$, the excess attenuation is 21.1 dB. It is interesting to note that much of the total excess attenuation is accumulated in front of the focal region. For example, the excess attenuation at $r = -10 \mu\text{m}$ for an initial intensity of $10,000 \text{ W/cm}^2$ is 13 dB. Because much of the excess attenuation occurs in the converging beam,

(a) 2.6 GHZ NITRØGEN 1000 W/CM SQ



(b) 2.6 GHZ NITRØGEN 1000 W/CM SQ

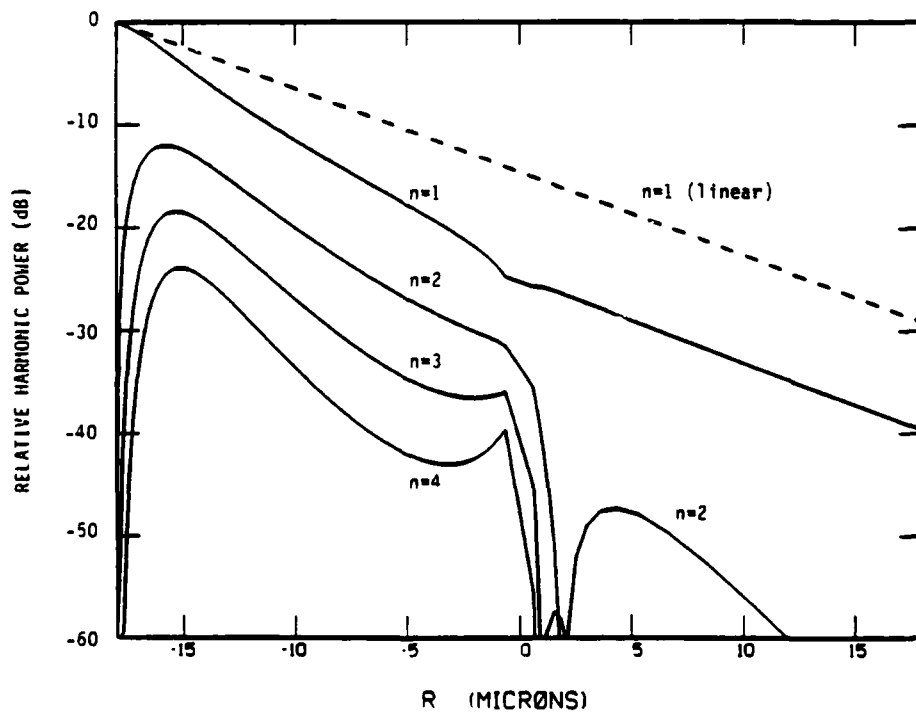
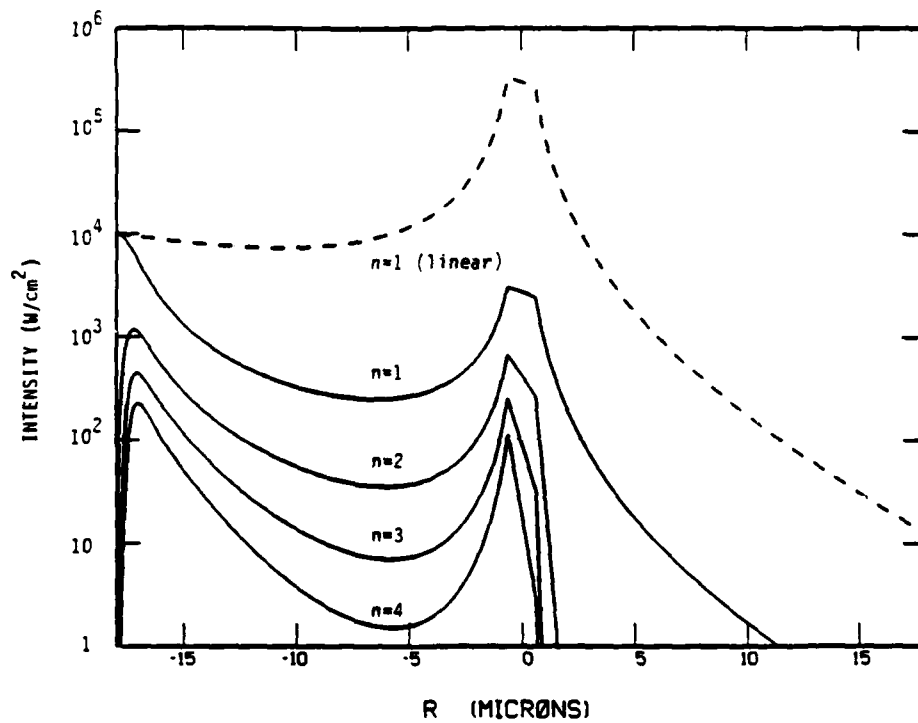


FIG. 8. Propagation of spherical waves in nitrogen for initial intensity of 1000 W/cm^2 . Plot (a) shows intensity of harmonics up to the 4th and (b) shows the distribution of power in the beam among the harmonics.

(a) 2.6 GHZ NITROGEN 10000 W/CM SQ



(b) 2.6 GHZ NITROGEN 10000 W/CM SQ

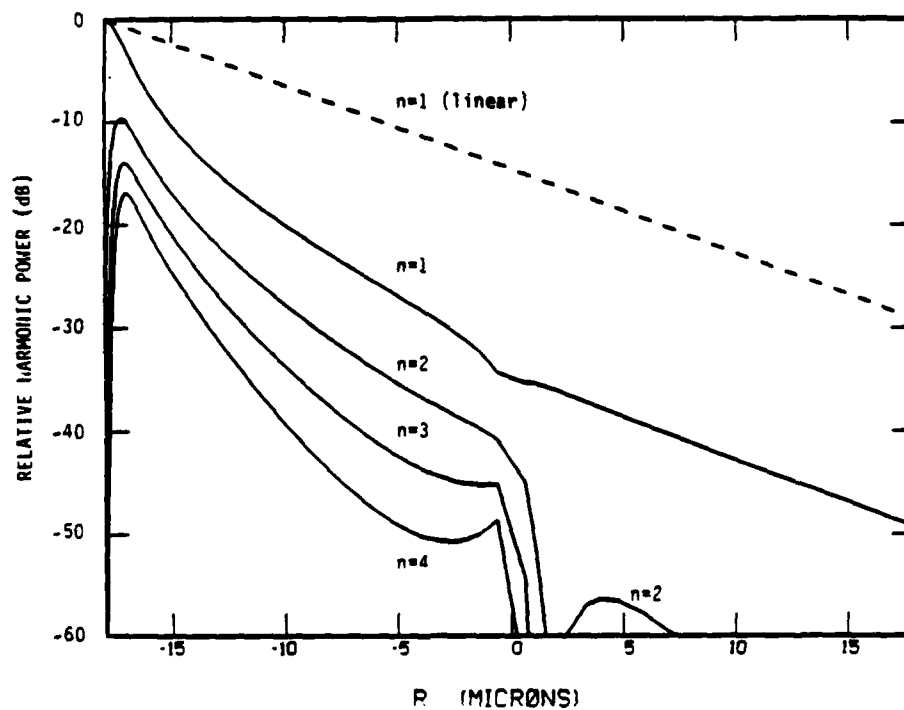


FIG. 9. Propagation of spherical waves in nitrogen for initial intensity of 10,000 W/cm². Plot (a) shows intensity of harmonics up to the 4th and (b) shows the distribution of power in the beam among the harmonics.

the intensity of the fundamental in the focal region changes by only 0.4 dB when the initial intensity is increased from 1000 W/cm² to 10,000 W/cm². The intensities of the higher harmonics in the focal region show a similar independence of initial intensity.

C.3.3 Calculation of harmonic amplitudes in water

The procedure used to compute harmonic amplitudes in liquid nitrogen can be applied to the case of propagation in 60°C water at 2.6 GHz. As before, an 18 μm lens radius is assumed. The parameters which change in the calculation include:

$$\begin{aligned} b &= 2\pi w_0^2/\lambda = 1.1 \mu\text{m} \\ w_0 &= .55 \lambda \\ \lambda &= .577 \mu\text{m} \\ \alpha_n &= n^2 \times 7.4 \times 10^4 \text{ m}^{-1} \\ B/A &= 5.7 \end{aligned}$$

Figure 10 shows calculated harmonic power in water for an assumed initial intensity of 1000 W/cm². The excess attenuation of the fundamental at the exit from the liquid ($r = 18 \mu\text{m}$) is observed to be small, approximately 1.5 dB. This is substantially less excess attenuation than seen in the liquid nitrogen case for the same initial acoustic intensity. This is expected based on the plane wave analysis summarized in Table 1.

Figure 11 shows calculated harmonic power in water for an initial intensity of 10,000 W/cm². The excess attenuation of the fundamental at $r = 18 \mu\text{m}$ is found to be 7.6 dB.

2.6 GHZ WATER 60C 1000 W/CM SQ

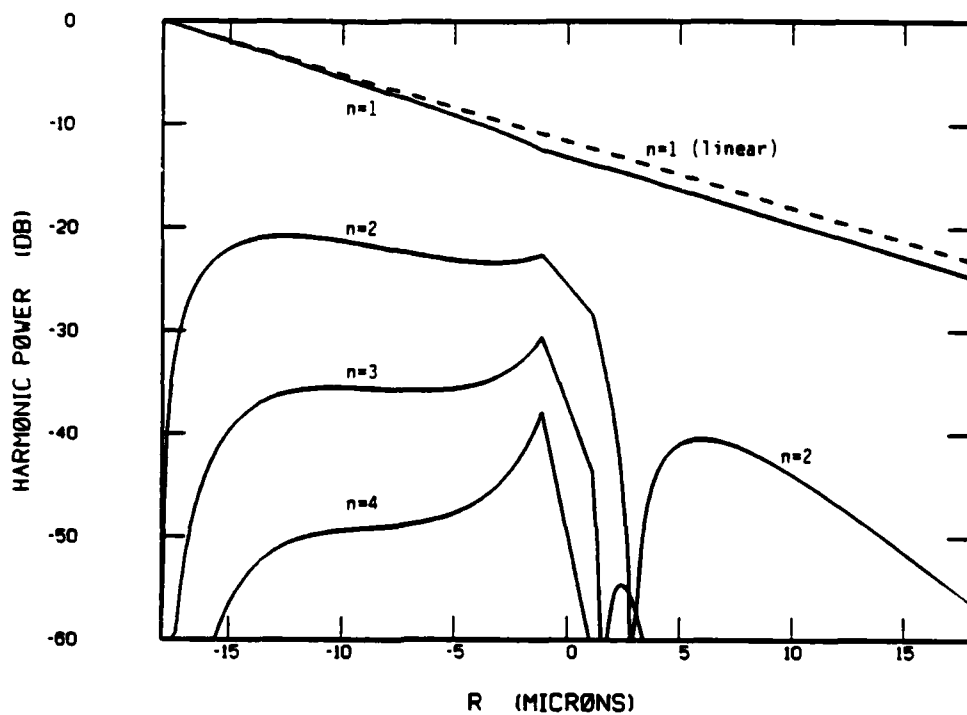


FIG. 10. Propagation of spherical waves in water for initial intensity of 1000 W/cm². The plot shows the distribution of power among the harmonics.

2.6 GHZ WATER (60C) 10000 W/CM SQ

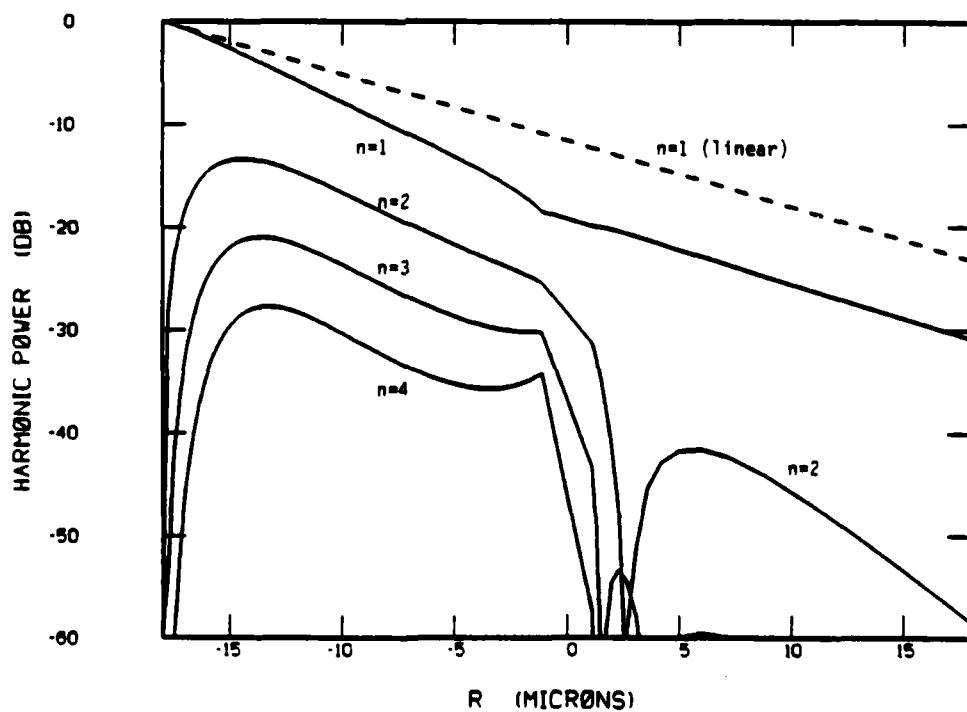


FIG. 11. Propagation of spherical waves in water for initial intensity of 10,000 W/cm². The plot shows the distribution of power among the harmonics.

C.3.4 Comparison of experimental and calculated values of excess attenuation

Using the nonlinear spherical wave analysis of the preceding sections, the excess attenuation of the fundamental can be calculated as a function of initial intensity and compared with experiment. Figure 12 shows plots of calculated and experimental results. The solid lines represent experimentally measured excess attenuation in nitrogen and 60°C water at 2.6 GHz as a function of RF input power. The solid dots in Fig. 12 are the calculated values of excess attenuation for a variety of initial intensities. It is found that if 1 milliwatt RF input power is assumed to be equivalent to 10 W/cm^2 at the lens surface, then a good fit between experimental and calculated points is obtained. The fact that both water and nitrogen curves are fit with the single adjustable parameter indicates that the basic features of nonlinear excess attenuation are accounted for in our calculations.

The correspondence between 1 mW RF input power and an acoustic intensity of 10 W/cm^2 is reasonable. To show this we perform a simple calculation. The surface area of an 18 μm radius lens with 53° opening half-angle is approximately $8.1 \times 10^{-6} \text{ cm}^2$. Thus an average intensity of 10 W/cm^2 corresponds to a total power of 0.08 milliwatts at the lens surface. This level of acoustic power is 11 dB smaller than the assumed lens rf input power of 1 mW. The loss of 11 dB from RF to acoustic power is a reasonable value and can be accounted for by assuming a one-way transducer conversion loss of 5 dB, a lens illumination loss of 5 dB and an acoustic impedance matching loss of 1 dB. Despite this good agreement between calculated and measured nonlinear excess attenuation, it should be noted that the calculated attenuation must necessarily underestimate the actual value since we have ignored the depletion which takes place in the focal region.

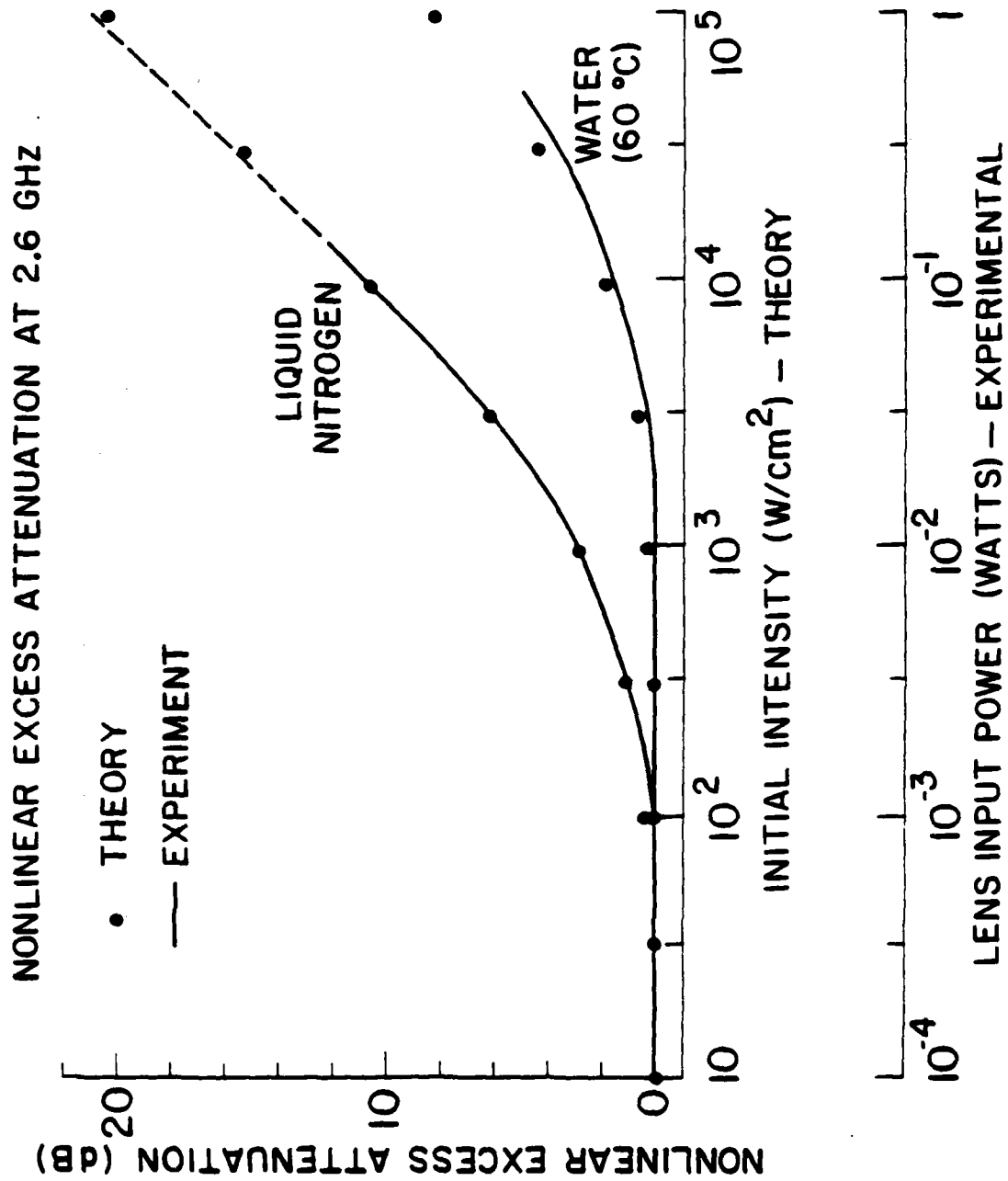


Fig. 12. Comparison of calculated and measured nonlinear excess attenuation.

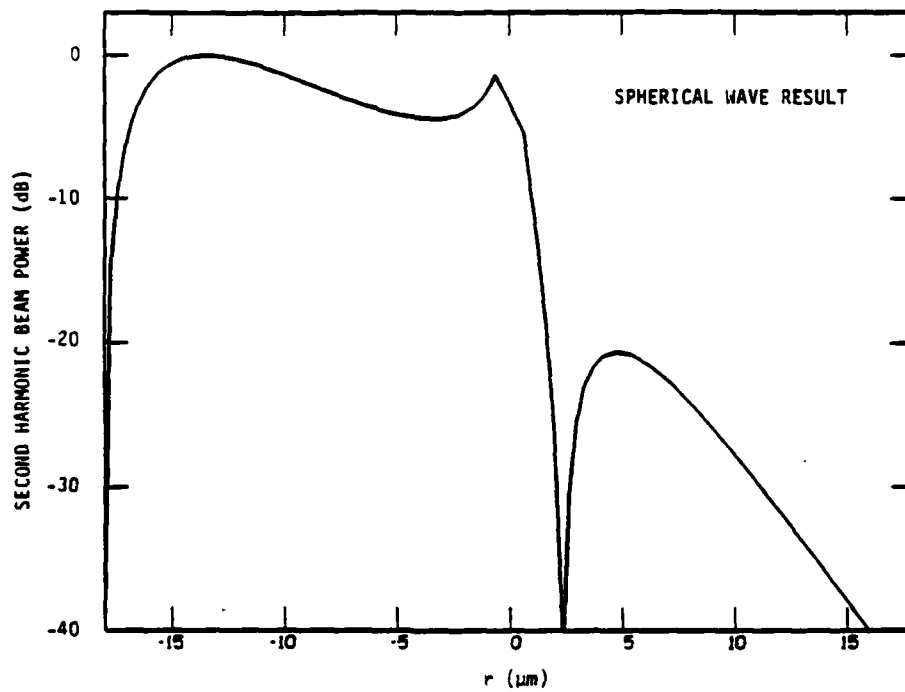
C.3.5 Connection between nonlinear spherical wave analysis and gaussian beam analysis

The most serious deficiency in the nonlinear spherical wave analysis is the neglect of nonlinear interaction in the region within one confocal length of the focus. In order to judge the significance of this approximation we compare the results of the spherical wave analysis with the results of the gaussian beam analysis of Section C.2. In order to make the comparison between the two methods we consider the case of very low initial acoustic intensity. In this limit the assumptions of negligible depletion of the fundamental and no significant generation of harmonics higher than the second are valid.

The plot in Fig. 13(a) shows the growth and decay of the second harmonic as computed by the spherical wave method. The assumed initial intensity in liquid nitrogen at 2.6 GHz was 1 W/cm^2 . This intensity level results in depletion of the fundamental by only 0.06 dB. The normalization of the curve is arbitrary. Figure 13(b) shows a comparison of the spherical wave method with gaussian beam analysis. The line of triangles is the spherical wave result and was copied from the plot in Fig. 13(a). The solid and dotted lines are the results of gaussian beam analysis and are the same as the lines shown in Fig. 5. The solid line is the total harmonic power, $|S|^2 = S_R^2 + S_I^2$. The dotted line is the component S_I^2 . It can be seen that agreement between the solid line and the spherical wave analysis (line of triangles) is good in the regions $-18 \mu\text{m} < r < -2 \mu\text{m}$ and $r > 12 \mu\text{m}$. Even more striking is the close agreement over the full range of r between the spherical wave analysis and the S_I^2 component of the gaussian analysis (dotted line).

The reason for the close agreement between the spherical wave analysis and S_I^2 can be understood as follows. S_I is the imaginary component of the

(a) 2.6 GHZ NITRØGEN 1 W/CM SQ



(b) COMPARISON OF SPHERICAL WAVE AND GAUSSIAN BEAM RESULTS

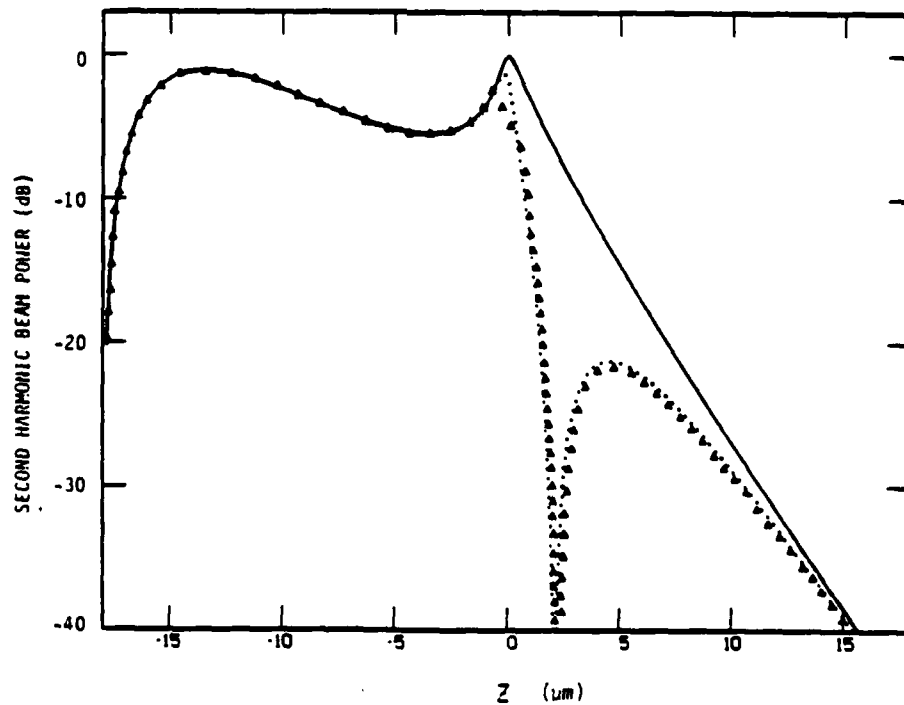


FIG. 13. Comparison of spherical wave and gaussian beam analyses. Plot (a) shows second harmonic power as calculated by the spherical wave method for a low initial intensity (1 W/cm^2). Plot (b) show comparison of the spherical wave result from (a) (triangles) with the gaussian beam result from Fig. 5 (solid and dotted lines). The solid line is S^2 which is proportional to second harmonic beam power. The dotted line is S_1^2 .

second harmonic wave as determined by gaussian beam analysis. As was seen in Section C.2, harmonic generation in the region far from the focus is in phase with the imaginary component. As the focal region is approached, however, the phase of the generation remains fairly constant until approximately one confocal length away from the focus. At this point, the phase changes more rapidly until at the focus the second harmonic generation is purely real. In other words, the second harmonic waves generated at the focus are 90° out of phase with waves arriving at the focus that were generated far "upstream". In the spherical wave analysis the gradually changing phase of the harmonic generation is ignored. Instead it is assumed that all generation occurring outside of one confocal length of the focus is in phase with waves generated "upstream" and all generation within one confocal length of the focus can be ignored. Thus the spherical wave analysis predominantly includes a component analogous to S_I and excludes the component analogous to S_R .

C.3.6 Contrast in the Nonlinear Focused Imaging System

The most interesting feature of imaging with high intensity focused acoustic waves is not that the generated higher harmonics focus to smaller spot sizes than the fundamental beam. This is a well understood and expected result. What is more surprising is the fact that the high resolution information contained by the higher harmonics is impressed onto the fundamental frequency, apparently with good efficiency. To explain this phenomenon we consider an idealized object consisting of two types of reflecting regions. One region is chosen to be perfectly reflecting; it reflects both the fundamental and higher harmonics with 100% efficiency and zero phase shift. The second region consists of a hypothetical material which perfectly reflects the fundamental wave and totally absorbs the higher

harmonics. If such an object were imaged at low power (linearly) by the acoustic microscope, we would expect to observe no contrast between the two regions. What we would like to know is how much contrast is observed if the object is imaged at high power.

To answer this question we use the nonlinear spherical wave analysis developed in this section. Consider the propagation of a focused beam with an initial intensity of 1000 W/cm^2 in liquid nitrogen at 2.6 GHz. The growth and decay of harmonics in such a beam was previously examined in Fig. 8 for the perfectly reflecting object. Figure 14 shows the results of the case where only the fundamental wave is reflected. The harmonic strengths in the converging beam are identical in Figs. 8 and 14. In the focal region of Fig. 14 we set the strength of all harmonics other than the fundamental to zero. We then calculate the behavior of the fundamental and higher harmonics in the diverging beam.

The contrast between the two types of reflecting regions is determined by the difference in strength of fundamental waves at the exit from the liquid ($r = 18 \text{ } \mu\text{m}$). To more easily compare the behavior of the fundamental waves we plot on a single graph in Fig. 15 the power in the fundamental for the two cases, as given by Figs. 8 and 14. We see that a significant difference in fundamental power appears in the diverging beam within several microns of the focal region. At the exit from the liquid the difference is 0.9 dB. Thus we have shown that imaging an object which has contrast for the higher harmonics also exhibits significant contrast at the fundamental frequency.

Although the above example is hypothetical, it is in some ways similar to real examples. Consider, for instance, a periodic grating of spatial frequency slightly higher than the cut-off frequency of linear imaging.

2.6 GHZ NITRØGEN 1000 W/CM SQ

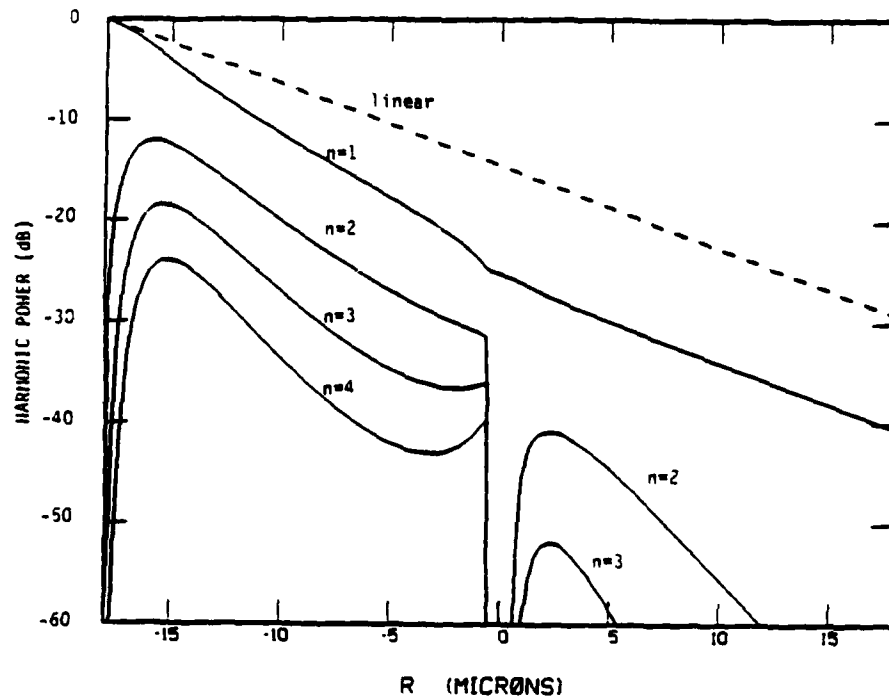


FIG. 14. Calculation of harmonic power for object which totally absorbs harmonics above the fundamental frequency. An initial intensity of 1000 W/cm^2 is assumed.

2.6 GHZ NITRØGEN 1000 W/CM SQ

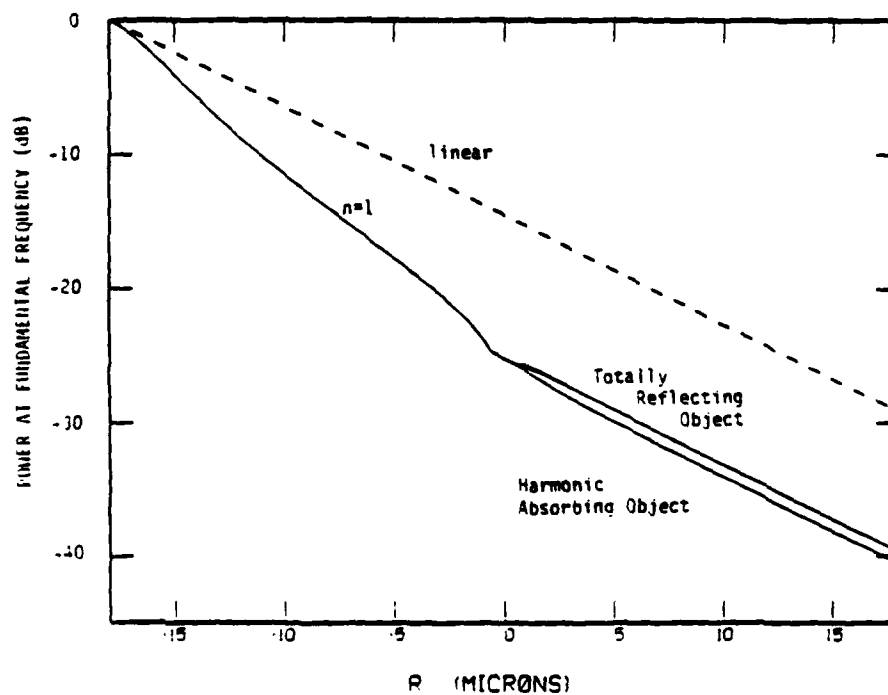


FIG. 15. Comparison of power in the fundamental for totally reflecting and harmonic absorbing objects. The contrast between these objects in the acoustic microscope is determined by the difference in fundamental power at the receiving lens ($r=18 \text{ } \mu\text{m}$).

Suppose the grating consists of perfectly reflecting and perfectly absorbing regions. For linear imaging, the strength of the received fundamental wave will be independent of where on the grating the focused beam is centered. The second and higher harmonics, however, will be a strong function of position of the beam on the grating since the spatial frequency of the grating lies within the spatial frequency response of the higher harmonics. Because the modulation of the higher harmonics affects the strength of the fundamental due to the nonlinear interaction, we expect that the grating can be detected at the fundamental frequency.

The experimentally observed contrast in nonlinearly resolved objects is found to be considerably greater than the 0.9 dB predicted by Fig. 15. For example, the contrast observed for the grating in Fig. 3 is approximately 3 dB. To explain the greater contrast it is probably necessary to take into account the nonlinear interaction in the focal region as well as the effect that such a complicated object has on the shape of the reflected wave fronts.

C.4. Summary of Nonlinear Imaging Results

We have seen that nonlinear interactions in the coupling liquid of the acoustic microscope are of great importance. One consequence of the nonlinear interaction is the improvement of imaging resolution which occurs when the microscope operates at high input power levels. The highest resolving power yet achieved in the acoustic microscope was achieved using the nonlinear resolution improvement discussed in this chapter. A grating with 2000 Å period was successfully imaged in liquid argon at 2.0 GHz. Even smaller gratings, perhaps as small as 1500 Å, could have been resolved at 2.8 GHz in nitrogen or argon had the gratings been available. A 3100 Å period grating was successfully resolved in hot water at 2.6 GHz. It is interesting

to note that this resolution is probably higher than the highest resolution yet achieved in water using conventional linear imaging.

An analysis of finite amplitude gaussian beams showed that the second harmonic spot size should be a factor of $\sqrt{2}$ smaller than the fundamental spot size. This is consistent with the experimental findings which set the lower bound of resolution improvement at a factor of 1.4. The gaussian beam analysis also indicated that a portion of the acoustic energy in the second harmonic is transferred into the fundamental beam after passage through the focal region. This result was corroborated by spherical wave calculations which showed that significant contrast will appear at the fundamental frequency for an object which modulates the intensity of the higher harmonics. In addition, the spherical wave calculations provided the basis for a detailed understanding of experimentally measured nonlinear excess attenuation.

REFERENCES

1. Status Report, 1 January - 1 July 1981, G.L. Report No. 3336.
2. Annual Summary Report, 1 July 1979 -- 30 June 1980, G.L. Report No. 3149.
3. Status Report, 1 July 1980 - 1 January 1981, G.L. Report No. 3241.
4. R.T. Beyer, Nonlinear Acoustics (Naval Sea Systems Command, Dept. of the Navy, 1974), Chapter 3.
5. D.T. Blackstock, J. Acoust. Soc. Am. 36, 534 (1964).
6. T.G. Muir, in Acoustical Imaging (Plenum, New York, 1981), Vol. 9, p. 93.
7. K.A. Naugol'nykh, S.I. Soluyan, and R.V. Khokhlov, Sov. Phys. Acoust. 9, 42 (1963).
8. N.S. Bakhvalov, Y.M. Zhileikin, E.A. Zabolotskaya, and R.V. Khokhlov, Sov. Phys. Acoust. 24, 10 (1978).
9. A.M. Sutin, Sov. Phys. Acoust. 24, 334 (1978).
10. D.A. Kleinman, A. Ashkin, and G.D. Boyd, Phys. Rev. 145, 338 (1966).
11. J.N. Tjøtta and S. Tjøtta, J. Acoust. Soc. Am. 69, 1644 (1981).
12. P.J. Westervelt, J. Acoust. Soc. Am. 35, 535 (1963).
13. V.P. Kuznetsov, Sov. Phys. Acoust. 16, 467 (1971).
14. E.A. Zabolotskaya and R.V. Khokhlov, Sov. Phys. Acoust. 15, 35 (1969).
15. F. Ingenito and A.O. Williams, J. Acoust. Soc. Am. 49, 319 (1971).
16. H. Kogelnik and T. Li, Appl. Optics 5, 1550 (1966).
17. D.H. Trivett and A.L. Van Buren, J. Acoust. Soc. Am. 69, 943 (1981).

EN

DAT
FILM

5

DTI